OPEN ACCESS

University of BRISTOL

Peer reviewed version

Link to published version (if available):
10.2514/6.2017-1355

Link to publication record in Explore Bristol Research
PDF-document

University of Bristol - Explore Bristol Research
General rights

Worst Case Gust Prediction of Highly Flexible Wings

R. G. Cook[*], D. E. Calderon[*], J. E. Cooper[†], M. H. Lowenberg[‡], and S. A. Neild[§]

University of Bristol, Queen's Building, University Walk, Bristol, BS8 1TR, United Kingdom

E. B. Coetzee[¶]

Airbus, Filton, Bristol BS34 7PA

In this work, the effect of aircraft flexibility on 1g and gust loads is investigated. A commercial aircraft with high aspect ratio wings (HARW) is generated as a baseline case using an in-house sizing tool, with variants of the aircraft created with a reduced stiffness via changes in skin thicknesses, including the associated mass reduction. These aircraft variants are modelled using an aeroelastic code based on an intrinsic beam theory in order to understand the effects of large, geometrically nonlinear deformations on the loads due to level flight and atmospheric turbulence in the form of "1-minus-cosine" gusts. The full, nonlinear results are compared to the same results obtained from the linear system and the linearised system to determine the limits of linear analyses on gust loads predictions. It was seen that reducing the wing stiffness on the baseline aircraft reduced 1g loads due to mass reduction, and also reduced the certain loads envelopes such as root torque and root bending moment by around 17% and 41%, respectively, compared to the baseline. Linear analyses consistently over-predicted these loads as well as the critical gust length, even for the stiffest cases, but severely under-predicted axial and fore-aft loads. However, the large deformations at 1g trim did not cause any round-the-clock gusts to become more critical than a purely vertical gust.

Nomenclature

1MC	1-minus-cosine
a	Body-fixed Reference Frame
A	Local Aerodynamic Reference Frame
B	Local Structural Reference Frame
$[C]$	Sectional Compliance Matrix
$[C^{xy}]$	Rotation matrix mapping from a variable in the y frame to the x frame
$\boldsymbol{F}$	Vector of Local Axial/Shear forces, $\{F_x; F_y; F_z\}$
F_x	Local Beam Axial force
F_y	Local Beam Fore-Aft Shear
F_z	Local Beam Vertical Shear
G	Global Reference Frame
g	Gust Reference Frame/Acceleration due to Gravity
$\boldsymbol{g}$	Acceleration due to Gravity
$\boldsymbol{\gamma}$	Vector of Local Strains
$\boldsymbol{H}$	Vector of Rotational Momenta
$\boldsymbol{\kappa}$	Vector of Local Curvatures
$\boldsymbol{M}$	Vector of Local Torsional/Bending Moments, $\{M_x; M_y; M_z\}$
M_x	Local Beam Torque

[*]Research Associate, Department of Aerospace Engineering, Queen's Building, University Walk, Bristol, BS8 1TR.
[†]Royal Academy of Engineering Airbus Sir George White Professor of Aerospace Engineering, AFAIAA.
[‡]Professor of Flight Mechanics, Department of Aerospace Engineering.
[§]Professor of Nonlinear Dynamics, Department of Aerospace Engineering.
[¶]Future Projects Office, Airbus Operations Ltd, Pegasus House Aerospace Avenue, Filton, Bristol, BS34 7PA.

American Institute of Aeronautics and Astronautics

M_y Local Beam Bending Moment
M_z Local Beam Fore-Aft Moment
m Sectional Mass per Unit Length
$[M]$ Sectional Mass Matrix
$\boldsymbol{\Omega}$ Local Rotational Velocities
$\boldsymbol{\omega}$ Body-Fixed Reference Frame Rotational Velocities
$\boldsymbol{P}$ Vector of Translational Momenta
$\boldsymbol{R}$ Position Vector from the origin of the body-fixed frame to the local beam frame
RTC   Round-the-Clock
s 1D curvilinear coordinate of a point along a deformed beam
$\boldsymbol{V}$ Local Translational Velocities
$\boldsymbol{v}$ Body-Fixed Reference Frame Translational Velocities

I.   Introduction

High aspect ratio wings can lead to significant fuel savings due to the reduction in induced drag, but also suffer from increased bending moments and resulting increase in structural weight. Typically such designs have little or no sweep and therefore the beneficial gust alleviation due to bending-torsion coupling inherent in sweptback designs is absent. They are also notoriously prone to nonlinear aeroelastic instabilities, and these nonlinear effects are usually not well understood; therefore the wing is often stiffened to avoid such instabilities with the penalty of further significant weight increases. The greater flexibility could also result in a strong coupling between structural dynamics and rigid body/flight mechanics modes and undesirable effects on the handling qualities. A further limitation on larger span designs are size restrictions on airport gates and ground handling.

<table>
<tr><td>(a) Airbus' Concept Plane[1]</td><td>(b) Boeing's Strut-Braced SugarVOLT Concept[2]</td></tr>
</table>

Figure 1: Future HARW Aircraft Concepts

A number of high aspect ratio wing configurations are being considered, and both Airbus and Boeing have published their own concept, as shown in Figure 1. The Boeing SUGAR Volt aircraft[3] includes a strut (to brace the wing) which will help reduce structural mass at the expense of additional drag. Other aspects such as the engine position (and type) need to be considered, as the engine could have a detrimental effect on the dynamics of a high aspect ratio wing. Technologies such as passive and active gust and manoeuvre load alleviation systems could also mitigate these effects.

In this work, the effect of flexibility on aircraft loads is investigated. To do this, a commercial aircraft is designed and sized using an in-house sizing tool. Using this as a baseline, the wing skin thickness is varied globally on the wing to produce flexible variants of the original aircraft. On the one hand this results in a weight reduction as the skin thickness is reduced, which is generally beneficial for an aerospace structure. Conversely, the structure becomes much more flexible, potentially resulting in large deflections which may enter the nonlinear regime. Geometrically nonlinear deflections can reduce loads due to vertical gusts by

American Institute of Aeronautics and Astronautics

reducing the gust velocity on out-board sections to a component of the velocity. However, lateral and round-the-clock (RTC) gusts are also required for certification loads, meaning that certain orientations of gust excitation may become more important in the gust loads analysis for highly-flexible aircraft. This study considers how mass reduction may affect gust loads. The effect of more flexible wings on the performance of the aircraft (lift-to-drag ratio or range, for example) will form the basis of a future paper.

This paper will first introduce the nonlinear aeroelastic approach used in this work, along with gust input definitions. After that, the specific aircraft model will be described, followed by 1g and dynamic gust loads analyses results with discussion. Finally, conclusions will be drawn.

II.   Aeroelastic Modelling

The methods used for modelling aeroelastic systems with nonlinear effects will be briefly described in this section. A definition of reference frames used in this study will be detailed. Then the structural model will be presented, followed by the aerodynamics. Finally, the implementation of the equations will be introduced.

A.   Reference Frame Definitions

In order to discuss the structural models, aerodynamic models and gust inputs, a number of reference frames need to be defined to clarify in which frame certain variables are expressed. Figure 2 illustrates a generic, highly flexible aircraft structure, and labels the reference frames.
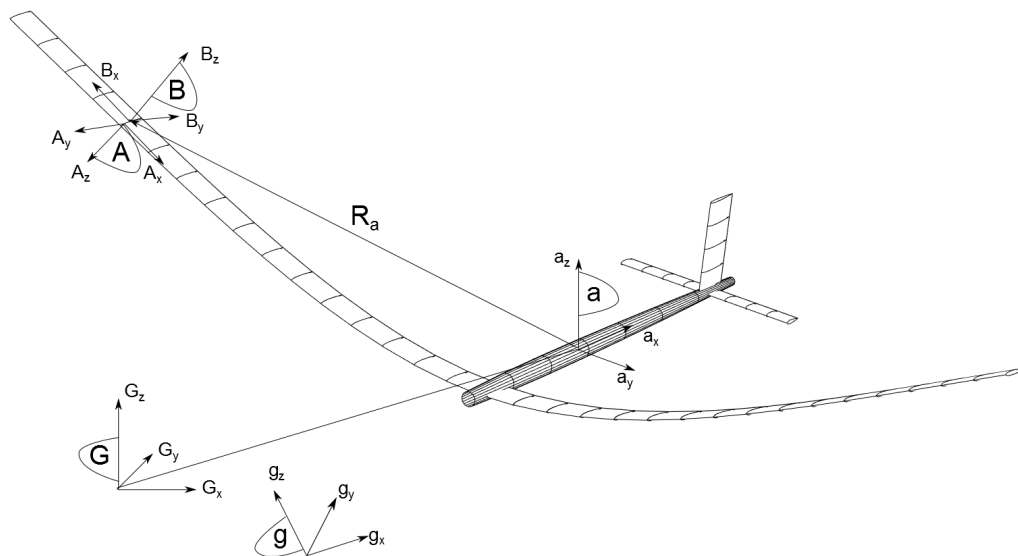

Figure 2: A diagram of the reference frames used in this work

1.   Global Reference Frame, G

The global reference frame, G, is an Earth-fixed inertial reference frame (assuming a flat and non-rotating Earth). The effect of gravity is expressed in this frame as a vector in the z-axis, $\boldsymbol{g} = [0; 0; -g]$, where g is the acceleration due to gravity.

2.   Body-Fixed Reference Frame, a

The body-fixed reference frame, a, is a reference frame that is free to move in translation and rotation within the global reference frame. It is, as its name suggests, rigidly fixed to a point on the aircraft, with

American Institute of Aeronautics and Astronautics

deformations of the structure defined relative to the body-fixed frame. For convenience, the origin of the body-fixed frame is chosen to be a point on the fuselage, with the x-axis aligned in the nose-to-tail direction.

3. Wing-Fixed/Local Reference Frame, B

The local reference frame, B, is a reference frame that is rigidly connected to the beam. All loads are given in this reference frame.

4. Aerodynamic Reference Frame, A

The aerodynamic reference frame, A is a reference frame that is rigidly connected to the beam, with the origin located at the aerodynamic centre of the aerofoil section at that beam location. It is convenient to define a separate reference frame for the aerodynamics to account for any rotations, such as twist or dihedral, that would mean that the aerodynamic reference frame was no longer coincidental with the local reference frame, B.

5. Gust Reference Frame, g

The gust reference frame, g, is introduced to simplify the gust description. It is a frame that can have an orientation and position independent of the global reference frame, G. In this frame, all gust velocities will be given as a purely vertical velocity vector in gust reference frame. The gust reference frame can then be oriented as required to produce variations of the gust.

B. Structural Modelling - Intrinsic Beam Formulation

The structural method used in this work is an intrinsic beam code, as presented by Hodges.[4] In this work, one considers a beam described simply by a 1D coordinate, s, along the deformed beam's length. The x-axis of the local reference frame B is parallel to the beam at any point.

To begin the beam description, it is first necessary to define the variables that are used in the formulation. First, local strain, $\boldsymbol{\gamma}_B(s,t) \in \mathbb{R}^{3\times1}$, and curvature, $\boldsymbol{\kappa}_B(s,t) \in \mathbb{R}^{3\times1}$, are defined as

$$\boldsymbol{\gamma}_B(s,t) = [C^{Ba}(s,t)]\boldsymbol{R}_a(s,t)' - \boldsymbol{e}_1 \tag{1}$$

and

$$\tilde{\boldsymbol{\kappa}}_B(s,t) = [C^{Ba}(s,t)][C^{aB}(s,t)]', \tag{2}$$

respectively. In these equations, $\boldsymbol{R}_a(s,t) \in \mathbb{R}^{3\times1}$ is the position vector to any point on the aircraft structure as seen in the body-fixed reference frame, and $[C^{Ba}(s,t)] \in \mathrm{SO}(3)$ is a rotation matrix mapping a vector in frame a to frame B. Additionally, $[C^{aB}(s,t)][C^{Ba}(s,t)] = I$. The vector $\boldsymbol{e}_1 := [1;0;0]$. The $\bullet'$ operator represents the spatial derivative of a certain variable with respect to s, while the $\tilde{\bullet}$ represents the cross-product matrix operator of a given vector.

Further to these strain and curvature definitions, the local translational velocity, $\boldsymbol{V}_B(s,t) \in \mathbb{R}^{3\times1}$, and angular velocity, $\boldsymbol{\Omega}_B(s,t) \in \mathbb{R}^{3\times1}$, are defined as

$$\boldsymbol{V}_B(s,t) = [C^{Ba}(s,t)]\left(\boldsymbol{R}_a(s,t) + \tilde{\boldsymbol{\omega}}_a(t)\boldsymbol{R}_a(s,t) + \boldsymbol{v}_a(t)\right) \tag{3}$$

and

$$\tilde{\boldsymbol{\Omega}}_B(s,t) = [C^{Ba}(s,t)][\dot{C}^{aB}(s,t)] + [C^{Ba}(s,t)]\tilde{\boldsymbol{\omega}}_a(t)[C^{aB}(s,t)], \tag{4}$$

respectively, where $\boldsymbol{v}_a$ is the translational velocity of the body-fixed reference frame, and $\boldsymbol{\omega}_a$ is the rotational velocity. The $\dot{\bullet}$ operator represents the temporal derivative of a certain variable. From this point on, the subscript B will be dropped from the velocities, strains and curvatures for clarity, as well as explicit mention that they are functions of beam location, s, or time, t.

The matrices $[M(s)] \in \mathbb{R}^{6\times6}$ and $[C(s)] \in \mathbb{R}^{6\times6}$ are introduced as the sectional mass and compliance matrices, respectively, and are given as

$$\begin{Bmatrix} \boldsymbol{P} \\ \boldsymbol{H} \end{Bmatrix} = [M] \begin{Bmatrix} \boldsymbol{V} \\ \boldsymbol{\Omega} \end{Bmatrix} = \begin{bmatrix} m & -m\tilde{\boldsymbol{\xi}}_{cg} \\ m\tilde{\boldsymbol{\xi}}_{cg} & J \end{bmatrix} \begin{Bmatrix} \boldsymbol{V} \\ \boldsymbol{\Omega} \end{Bmatrix} \quad \text{and} \quad \begin{Bmatrix} \boldsymbol{\gamma} \\ \boldsymbol{\kappa} \end{Bmatrix} = [C] \begin{Bmatrix} \boldsymbol{F} \\ \boldsymbol{M} \end{Bmatrix} = \begin{bmatrix} c_{\gamma f} & c_{\gamma m} \\ c_{\kappa f} & c_{\kappa m} \end{bmatrix} \begin{Bmatrix} \boldsymbol{F} \\ \boldsymbol{M} \end{Bmatrix} \tag{5}$$

which maps velocities to translational and rotational momenta, $\boldsymbol{P}$ and $\boldsymbol{H}$, respectively, and forces, $\boldsymbol{F}$, and moments, $\boldsymbol{M}$, to strains and curvatures. It can be seen that the relationship between the beam forces and moments, and the strains and curvatures is a linear one, indicating that there are no material nonlinearities such as skin-buckling accounted for in this method.

The equations of motion of the beam are,[4]

$$[M]\begin{Bmatrix}\dot{\boldsymbol{V}}\\\dot{\boldsymbol{\Omega}}\end{Bmatrix} + \begin{bmatrix}\tilde{\boldsymbol{\Omega}} & 0\\\tilde{\boldsymbol{V}} & \tilde{\boldsymbol{\Omega}}\end{bmatrix}[M]\begin{Bmatrix}\boldsymbol{V}\\\boldsymbol{\Omega}\end{Bmatrix} = \begin{Bmatrix}\boldsymbol{F}'\\\boldsymbol{M}'\end{Bmatrix} - \begin{bmatrix}\tilde{\boldsymbol{F}} & 0\\\tilde{\boldsymbol{M}} & \tilde{\boldsymbol{F}}\end{bmatrix}[C]\begin{Bmatrix}\boldsymbol{F}+\boldsymbol{e}_f\\\boldsymbol{M}\end{Bmatrix} + \begin{Bmatrix}\boldsymbol{f}\\\boldsymbol{m}\end{Bmatrix},\tag{6}$$

where $\boldsymbol{e}_f = c_{\gamma f}\boldsymbol{e}_1$.

In Eq. 6, the degrees of freedom of the equations of motion are local velocities and strains and curvatures. In contrast to similar methods which rewrite the equations of motion purely in terms of strains and curvatures, or alternatively in terms of displacements and orientations, the intrinsic beam approach introduces an additional equation which relates the velocities to the strain and curvatures, which closes the formulation. The equation to close the formulation, derived from Eqs. 1 and 2, is

$$[C]\begin{Bmatrix}\dot{\boldsymbol{F}}\\\dot{\boldsymbol{M}}\end{Bmatrix} = \begin{Bmatrix}\boldsymbol{V}'\\\boldsymbol{\Omega}'\end{Bmatrix} - \begin{bmatrix}\tilde{\boldsymbol{\Omega}} & \tilde{\boldsymbol{V}}\\0 & \tilde{\boldsymbol{\Omega}}\end{bmatrix}[C]\begin{Bmatrix}\boldsymbol{F}+\boldsymbol{e}_f\\\boldsymbol{M}\end{Bmatrix}.\tag{7}$$

One final equation of motion is required for the free-flying aircraft,

$$\int_0^s \begin{bmatrix}I & 0\\\tilde{\boldsymbol{R}}_a & I\end{bmatrix}\begin{bmatrix}C^{aB} & 0\\0 & C^{aB}\end{bmatrix}\left([M]\begin{Bmatrix}\dot{\boldsymbol{V}}\\\dot{\boldsymbol{\Omega}}\end{Bmatrix} + \begin{bmatrix}\tilde{\boldsymbol{\Omega}} & 0\\\tilde{\boldsymbol{V}} & \tilde{\boldsymbol{\Omega}}\end{bmatrix}[M]\begin{Bmatrix}\boldsymbol{V}\\\boldsymbol{\Omega}\end{Bmatrix}\right)ds = \begin{Bmatrix}\boldsymbol{f}_a\\\boldsymbol{m}_a\end{Bmatrix},\tag{8}$$

which satisfies the conservation of momentum equations for the beam, or set of beams, in the G reference frame. The velocity of the rigid body is coupled with the beam equation as a velocity boundary condition on Eq. 7 at the root.

The intrinsic beam formulation results in double the number of variables compared to alternative nonlinear beam approaches, but in doing so retains a much more algebraically simple set of equations to solve. Palacios et al[5] compare the intrinsic beam formulation to two common approaches to nonlinear beam modelling, namely displacement-based[6] and strain-based methodologies,[7] and highlights benefits and drawbacks of each method. The simplicity of the intrinsic beam equations can be seen to be an advantage computationally.

A finite-element (FE) approach to the solution of the intrinsic beam equations is applied. Here, piecewise-linear shape functions are used in a scheme similar to those used in Hodges et al.[8] However, rather than using a mixed-formulation, the intrinsic beam equations are solved for velocities, and strains and curvatures directly. The position and orientation of the beam can then be obtained by the spatial integration of the strains and curvatures, or the temporal integration of the velocities. In this work, the former approach is used for the static solutions, with the latter approach then used used for dynamic results. The orientations of the beam are parameterised using quaternions.

As part of on-going validation of nonlinear codes at the University of Bristol, this particular implementation has been compared in terms of accuracy and computation times with a number of alternative nonlinear beam formulations. Previous comparisons and summaries of all the beam models for static aeroelastic analyses was made in Howcroft et al.[9]

Comparisons for static results are also made with MSC.NASTRAN, but not for the dynamic aeroelastic system, the reason for which is explained in the next section.

C.   Aerodynamics

To apply representative aerodynamic forces to the structural model, an unsteady strip theory is used. Strip theory has been shown in the literature to provide a reasonable approximation to aerodynamic forces for HARW, but lacks the induced drag terms and 3-dimensional effects that DLM, VLM and UVLM methods can provide. Nonetheless, the computational speed of strip theory allows for rapid assessment of numerous cases, and gives a useful insight into aeroelastic phenomena.

Unsteady effects are included into the strip theory approach used here via Leishman's indicial response method[10] (using Jones' approximation to Theodorsen's function[11]). Palacios et al[5] showed how Leishman's two-state approach was comparable in terms of accuracy to other methods such as Peters' Finite-State

approach[12] requiring 4-8 states, with the obvious benefit of a vastly reduced number of aerodynamic states. The aerodynamic forces and moments are determined from the local beam velocities and local velocity fields due to gust disturbances, and enter into the structural equation, Eq. 6.

Static lift slopes are calculated from a VLM solver to provide realistic 3D tip loss effects into the strip-theory approach.

D. Numerical Implementation

The equations of motion are solved in MATLAB. The static solver uses a Newton-Raphson method to solve the FE discretisation of Eq. 6 with velocities and time derivatives set to zero. The total state size of the static system is therefore $6n$, where n is the number of elements of the system.

The dynamic solver solves Eqs. 6 and 7 simultaneously with Eq. 8, along with velocity integration equations and aerodynamic unsteady equations, using a Newmark-β time-stepping solver. The total state size of the free-flying beam system is $12n + 6$, with an additional $7n$ states for temporal velocity integration to obtain positions and orientations, and a further $2n$ states for the unsteady aerodynamics states, resulting in a total of $21n + 6$ states.

E. Gust Loads Process

In order to determine the loads on the aircraft due to exogenous gust disturbances, a gust loads process is required. The specific gust loads process used in this work is defined here.

In a standard industrial gust loads process on a linear aeroelastic system, the 1g loads at trim condition and the additional incremental gust loads can be calculated separately and added together in post-processing due to the linear approximations of the model.[13] Furthermore, only vertical and lateral gusts need to be calculated, with negative and round-the-clock gusts also determined in post-processing. Supposing that a certain load has been determined from a vertical and lateral gust load case (obtaining $L_{n_{VERT}}$ and $L_{n_{LAT}}$, respectively), the load from a gust orientated at θ from the vertical can be determined simply as,

$$L_{n_\theta} = L_{n_{VERT}} \cos\theta + L_{n_{LAT}} \sin\theta \tag{9}$$

Therefore, the maximum gust is some combination of these gusts orientated at an angle θ_{RTC} calculated as

$$\theta_{RTC} = \tan^{-1}\left(\frac{L_{n_{LAT}}}{L_{n_{VERT}}}\right) \tag{10}$$

and the maximum loads are calculated as

$$L_{n_{RTC}} = \sqrt{L_{n_{VERT}}^2 + L_{n_{LAT}}^2} \tag{11}$$

In contrast for a nonlinear system, gust loads must be calculated on the aircraft in its trim configuration to correctly account for large deformations and the effect this has on the aerodynamic forces, gravity forces and flight dynamics of the aircraft. It also means that round-the-clock gusts can no longer be determined from the vertical and lateral gusts alone, as in Eqs. 10 and 11.

The gust loads process followed in this work considers discrete gust events, in the form of "1-minus-cosine" (1MC) disturbances. The aircraft is trimmed, and subjected to a family of 1MC gusts with the velocity magnitudes and gust lengths defined by FAA[14]/EASA[15] guidelines. For this gust, the velocity profile in the gust reference frame, g, is defined as

$$\boldsymbol{w}_g = \begin{bmatrix} 0 \\ 0 \\ \frac{1}{2} w_{g_{max}} \left(1 - \cos\left(\frac{\pi x}{H}\right)\right) \end{bmatrix} \tag{12}$$

where H refers to the gust gradient (half the gust length), x is distance into the gust disturbance, and $w_{g_{max}}$ is a gust intensity value determined from the FAA/EASA regulations.[14,15] An illustration of the gust intensity as a function of distance into the gust event for the series of gust gradients in this study is plotted in Figure 3.

Vertical and lateral gusts are considered, as well as combinations of vertical and lateral gusts which give a rough indication of whether round-the-clock gusts may form critical elements of the loads envelope. For
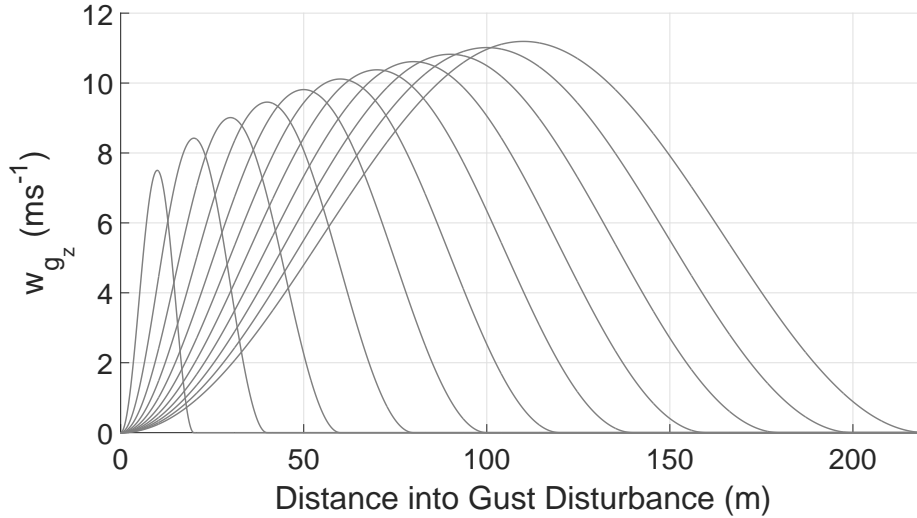
American Institute of Aeronautics and Astronautics

Figure 3: A series of 1-minus-cosine gust inputs for an altitude of 9,000m.

a vertical gust, the gust reference frame, g, coincides with the global reference frame, G. If the aircraft is initially trimmed with a velocity purely in the global reference frame's x-axis, the gust reference frame, g, is rotated about the x-axis by an angle θ for the gust disturbances in different directions. Therefore, $\theta = 0°$ refers to a positive vertical gust, $\theta = 90°$ refers to a lateral gust, $\theta = 180°$ refers to a negative vertical gust, etc.

Therefore, in total, 11 gust gradients (10m-110m in 10m increments), 13 gust directions (0°-360° in 30° increments), and 6 flexibility variants are considered. Not all gust directions need to be simulated due to the lateral symmetry of the aircraft, so the number of gust directions can be reduced to 7 (0°-180° in 30° increments), with the left and right wing loads reflected to provide the rest of the results. Therefore, 462 simulations need to be run for the nonlinear case. Only vertical and lateral gusts (0° and 90°) are required for the linear and linearised cases, resulting in only 132 simulations each.

Comparisons of the interesting quantities (IQs) obtained from the full nonlinear simulations are made with results from the linear, and linearised system. The linear results are obtained by simulating an undeformed aircraft with no gravitational forces, subjected to gusts of a greatly reduced intensity (scaled down such that the system remains in the linear regime); loads are obtained by rescaling the response and adding the 1g loads. The linearised results are obtained by running the deformed aircraft through a similarly scaled family of gusts; loads are calculated by removing the 1g loads, rescaling the loads, and replacing the 1g loads. It should be noted that for the linear and linearised loads obtained from the intrinsic beam approach, the 1g loads are obtained from a nonlinear static solver. The reason behind doing linear and linearised results this way, as opposed to using MSC.NASTRAN for comparison purposes, is simply to avoid any differences in behaviour due to different aerodynamics or solution approaches. Kier[16] for example has illustrated how different aerodynamic approaches can impact the loads; differences which may detract from the underlying trends in this work by comparing a linear structural model with DLM aerodynamics to a nonlinear structural model with strip theory.

III.   Aircraft Model

The focus of this particular gust loads study is on a high-aspect ratio, commercial airliner-type aircraft configuration, similar to those currently considered in industry.[1,3] Therefore, a representative aircraft has been designed which features similar characteristics as contemporary concept aircraft. The aircraft wing is fixed to the fuselage rigidly at the root, and does not feature any strut bracing, in contrast to the SugarVOLT.[3]

The planform properties of the aircraft are presented in Table 1. There is also an elevator on the HTP which is 25% of the chord and runs along the full length of the HTP.

The baseline aircraft wing is sized using an in-house sizing tool, which generates an optimum wing and

American Institute of Aeronautics and Astronautics

tail box structure for a range of static loads cases. A rendering of the aircraft can be seen in Figure 4. The wing-box is then reduced to a beam-like structure for use in the intrinsic beam formulation.

Planform Property	Wing	HTP	VTP
Taper Ratio	0.25	0.35	0.35
Total Area (m^2)	130	27.46	13.73
Root chord (m)	4.30	3.48	3.48
Total Span (m)	48.38	11.70	5.85
Aspect Ratio	18	5	5
1/4-chord sweep (°)	12	20	20

Table 1: Planform properties of the baseline aircraft used in this study
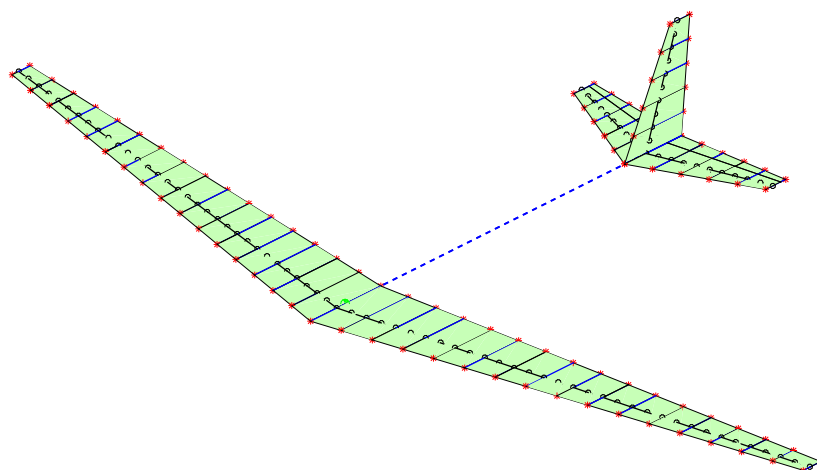
Figure 4: An illustration of the aircraft used in this study

Flexibility variants are then generated by changing the skin thickness of the baseline aircraft wing box by a factor, referred to in this paper as the 'flexibility factor'. The sectional stiffness properties in bending, EI, and torsion, GJ, are plotted in Figure 5 for various flexibility cases. It can be seen that between the stiffest and most flexible cases considered, the in-plane and out-of-plane bending stiffness reduces by around an order of magnitude at the root, indicating a significant reduction. The torsion, however, only reduces by a factor of 2. It is assumed that the fuselage is rigid, and the HTP and VTP stiffnesses are not changed throughout the analysis. We are ignoring the effect that the change in thickness has upon the stress and buckling behaviour, as the emphasis of the study is on the effect of changes in stiffness on the dynamic response. Of course, for a real world aircraft design, the process presented here would be used as part of sizing process or optimisation to ensure critical stresses were not exceeded.

One mass and flight case will be considered for this study. The total mass of the baseline aircraft is 61,442kg, which is comparable to the MZFW of a short- to medium-range commercial aircraft. The centre of gravity position of the whole undeformed baseline aircraft lies 0.51 metres behind the wing beam. The aircraft is flown at an altitude of 9,000m at a Mach number of 0.7. Compressibility effects are not included in the aerodynamic models. Each wing is modelled with 16 equal length elements, and each HTP and the VTP are modelled with 5 elements each, totalling 47 elements in total. For the dynamic system this corresponds to a state size of 993 for the structural dynamics, velocity integration and unsteady aerodynamics equations.
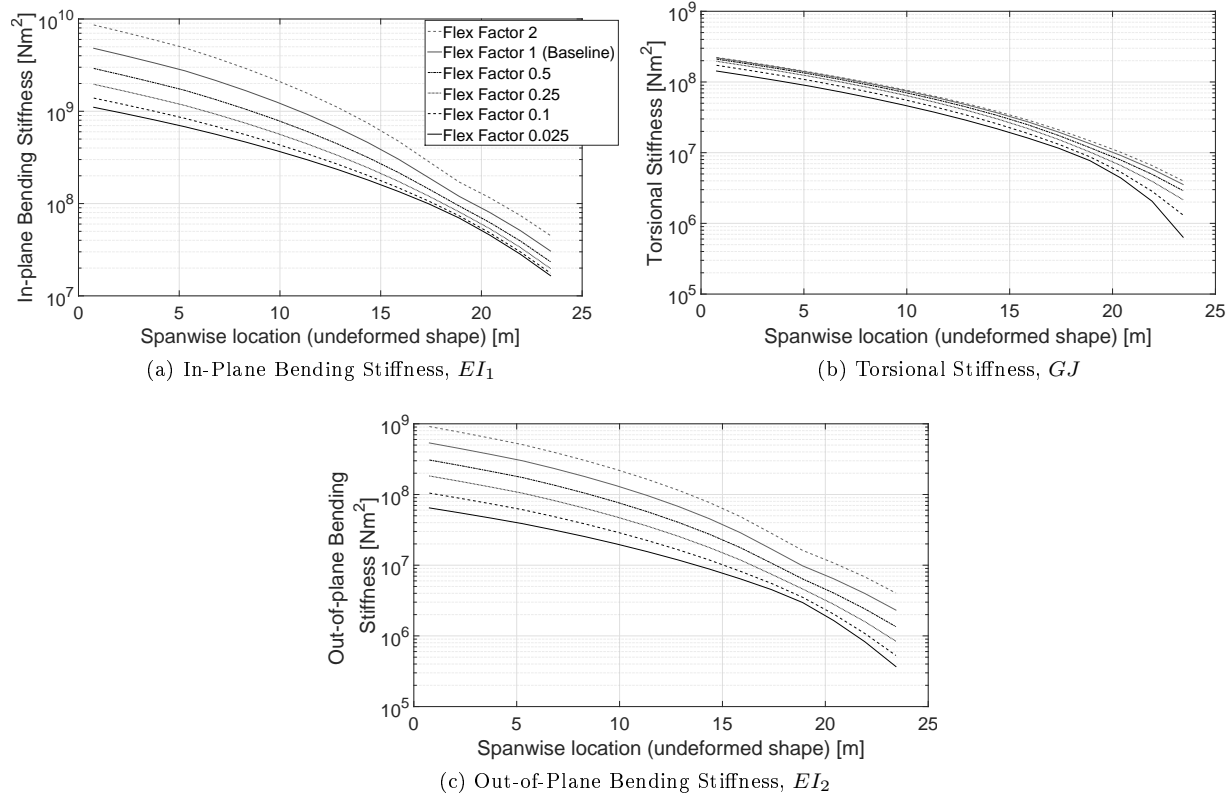
(a) In-Plane Bending Stiffness, EI_1

(b) Torsional Stiffness, GJ

(c) Out-of-Plane Bending Stiffness, EI_2

Figure 5: Wing stiffness data

IV.   Results

In this section, the results from the gust loads analysis are presented. First, the static behaviour of the aircraft for different flexibility cases is shown, followed by the dynamic gust loads results.

A.   Static 1g Loads

The aircraft is first trimmed using the elevator to obtain the 1g loads, flight shape and angle of attack for a series of flexibility cases - these are necessary to provide the nonlinear simulation with the initial conditions to perform gust loads. The trim condition is determined using a static lift and moment balance. Thrust is not required for the force balance, due to a lack of any drag force in the aerodynamics modelling.

Trim angles of attack and elevator deflections are shown in Figure 6. It can be seen how the angle of attack and elevator deflection initially reduces as the aircraft becomes more flexible, but then rapidly increases as the rigidity continues to reduce. The results match well with MSC.NASTRAN for the angle of attack. However, there is a clear difference in elevator deflection which is simply due to differences in elevator lift and moment curve slopes. The resulting tip vertical displacement at trim condition is also plotted in Figure 6 (as seen in the body-fixed reference frame), showing an excellent match between MSC.NASTRAN and the intrinsic beam approach for the stiffest wing considered, where the static deflections are still in the linear regime. The difference between the linear and nonlinear approaches can then be seen as the aircraft becomes more flexible. The overall trim shape of the left wing as seen in the flight direction is plotted in Figure 7. Again, a good match can be made to MSC.NASTRAN for the stiffest case, and furthermore it can be seen how at the most flexible cases a significant degree of tip shortening can be observed due to geometrically nonlinear deformations. For the most flexible case, the tip deflection exceeds 25% of the wing span; from an earlier study[9] it was seen that nonlinear behaviour should be expected from deflections of that size.

The distributed 1g trim loads on the wing are plotted in Figure 8 for a selection of flexibility variants,
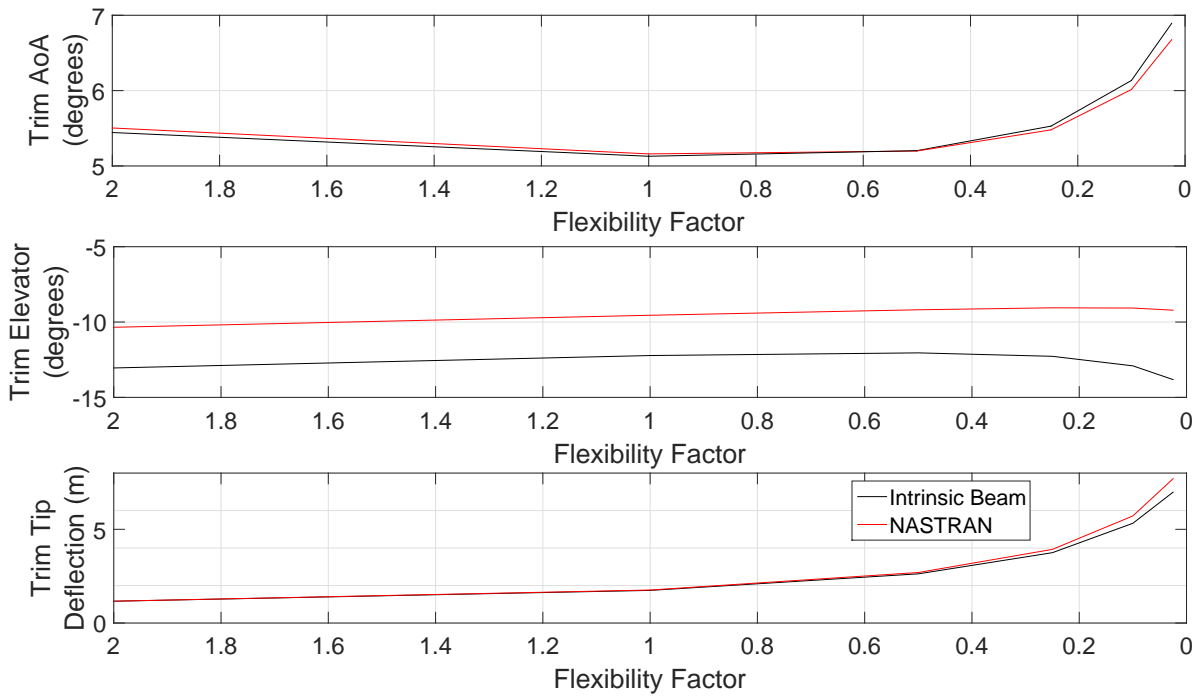
Figure 6: Trim Angle of Attack, elevator deflection and tip displacement vs. flexibility factor, comparing Intrinsic Beam results with MSC.NASTRAN
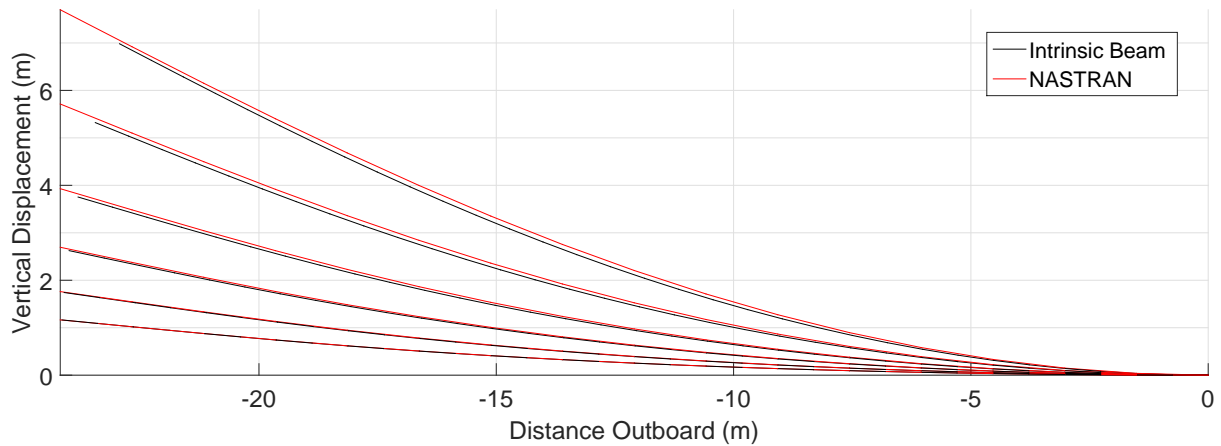

Figure 7: 1g left wing flight shapes for various flexibility factors, comparing Intrinsic Beam results with MSC.NASTRAN

comparing nonlinear results from the intrinsic beam method to MSC.NASTRAN. It can be seen how for vertical shear, F_z, the root value decreases with flexibility factor, consistent with the mass reduction of the aircraft. Vertical shear, F_z, and bending moment, M_y, match well between the intrinsic beam model and MSC.NASTRAN, particularly for the values near the root of the stiffest wing. The torsion moment, M_x, shows a more notable difference between nonlinear and linear analyses, due mainly to differences in the orientation of the aerodynamics lift vector with respect to the local reference frame between the two methods which generates a pitch down torque in the intrinsic beam formulation. Most obviously, it can be

seen that there are considerable axial forces, F_x, fore-aft shear, F_y, and in-plane moments, M_z, developed in the nonlinear analysis which are exactly zero in the linear analysis, again due to the orientation of the lift vector. This was also noticed in an earlier study.[9]
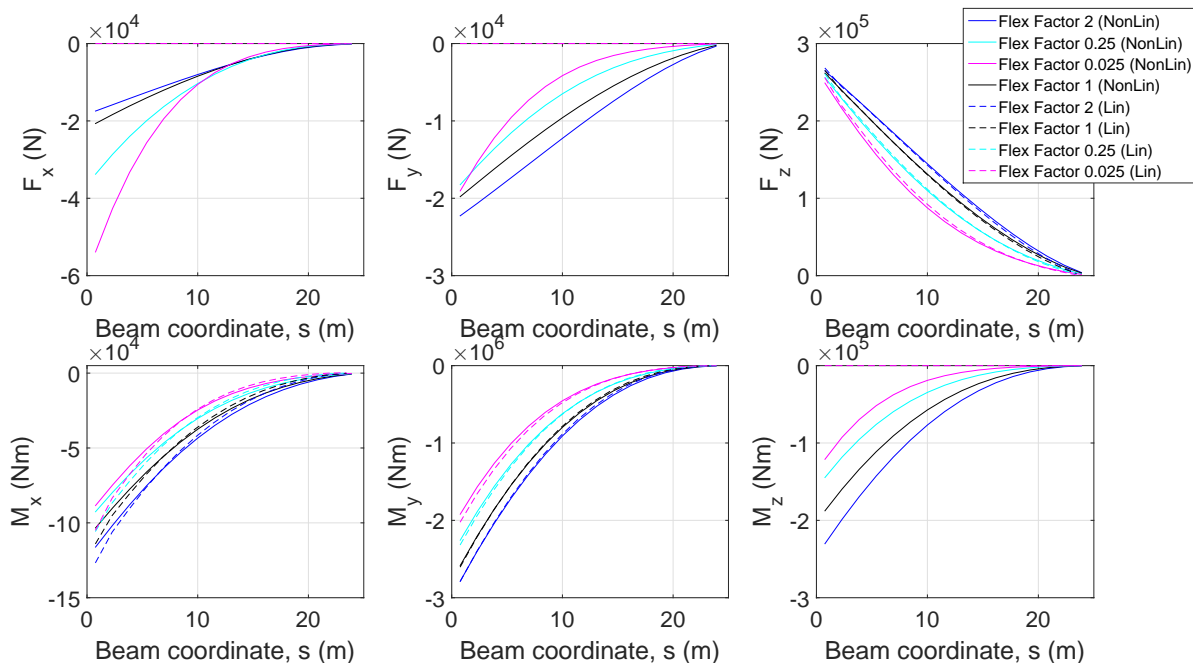

Figure 8: Wing trim local loads distributions, plotted against local beam coordinate (see Figure 2 for load directions)

B. Dynamic Gust Loads

The dynamic gust results are now presented. The nonlinear aeroelastic system is subjected to a family of 1MC gust disturbances for a variety of flexibility cases and various gust directions, along with linear and linearised system responses. Due to the number of types of gust disturbance (different gust lengths/gust directions) applied to the different flexibilities of aircraft, envelopes of the gust response are made with respect to a certain variable in order to highlight trends and features.

An example response of the root loads on the nonlinear system to a vertical family of 1MC gust disturbances can be seen in Figure 9, comparing the stiffest wing to the most flexible. A few qualitative differences can be observed, for example, the torsion response has significant high frequency content when hit by the shortest gusts due to coupling with a flexible bending mode of the HTP. The HTP bending mode excites the fuselage in pitch, which excites the torsion mode of the wing; it is more pronounced in the flexible case due to the higher trim deformations lowering the effective rotational inertia. A longer simulation reveals that the oscillation does decay eventually, but is very lightly damped. Additionally, it can be seen that the maximum bending load is due to the second overshoot on the stiffer case, but due to the first peak on the more flexible case. Moreover, the difference between the maximum and minimum loads is reduced as the aircraft becomes for flexible, as well as just the 1g loads as seen in Figure 8. This loads reduction is due to the large wing tip orientations reducing the effective angle of attack due to gust velocity.

The gust response in Figure 9 is due to a purely vertical gust where the large rotations can reduce loads compared to an undeformed configuration. However, a gust profile could exist which is rotated by some angle to vertical and could potentially result in larger loads, especially if the wing exhibits large deformations and rotations. Therefore it is important to consider angled gusts also. Gust loads from angled gusts can be visualised by determining the maximum and minimum loads of the gust family for a particular gust orientation, and plotting them in a polar plot. Root torsion and bending loads for a full 360° sweep (in 30° increments) are plotted in Figure 10 for the stiffest and most flexible aircraft variants. For both the stiffest and most flexible cases, the differences seen between maximum and minimum are biggest at 0° and
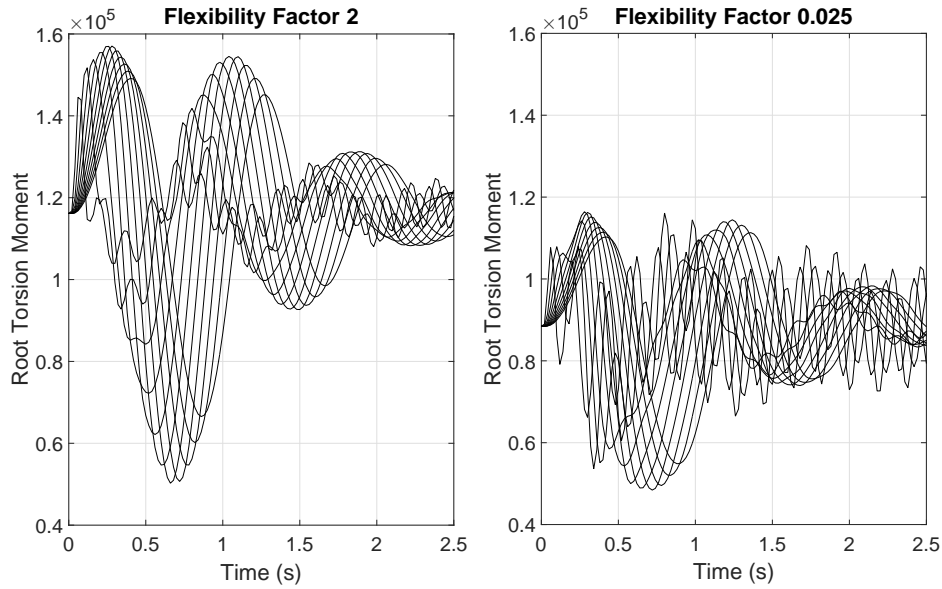
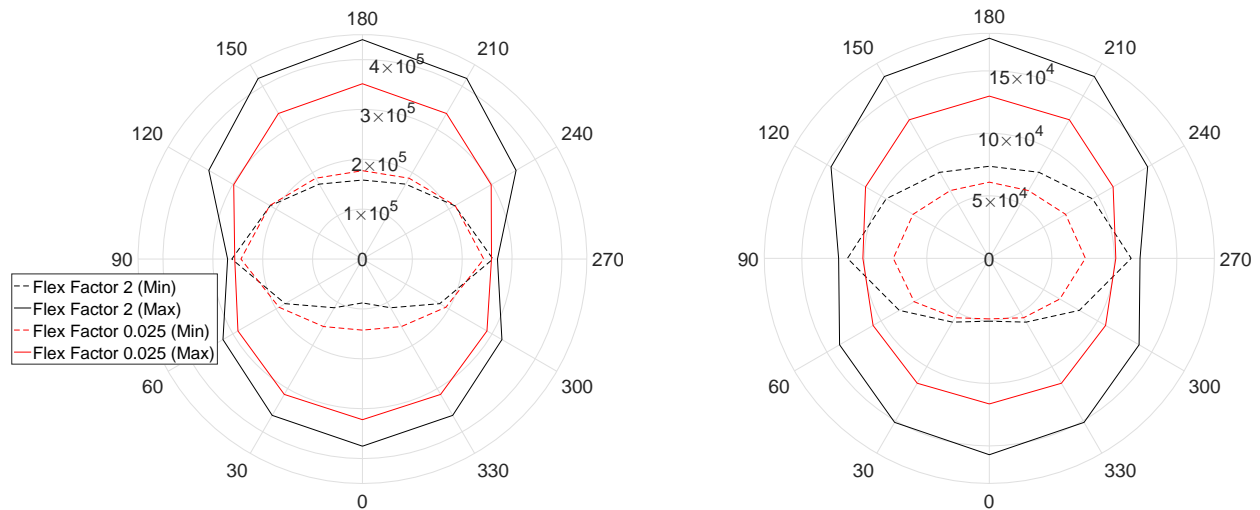(a) Root torsion moment, M_x, gust response (absolute value)
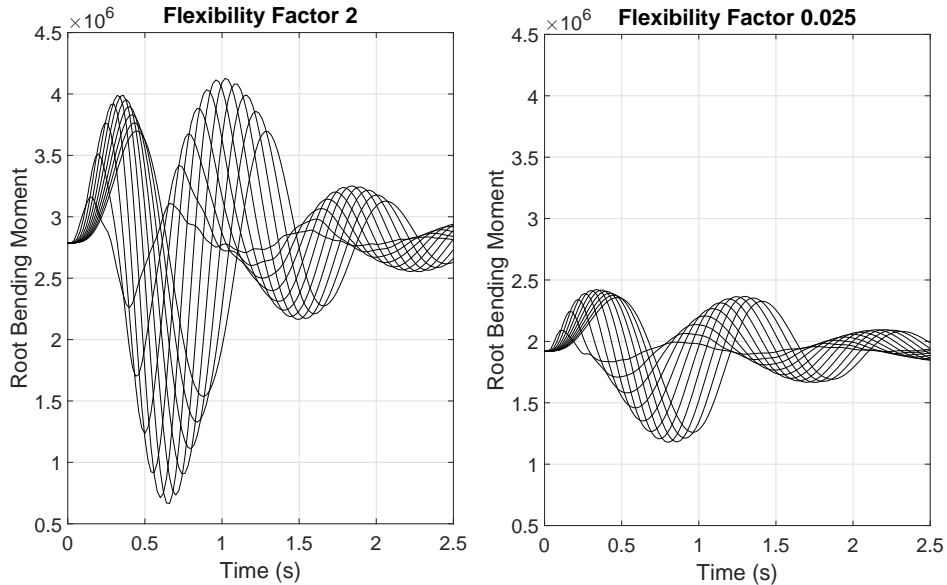
(b) Root bending moment, M_y, gust response (absolute value)

Figure 9: Example gust family response

180°, and smallest at 90° and 270°, but it can be seen that the gap between maximum and minimum loads for the 90° and 270° gusts is much larger for the more flexible cases due to the large wing deformations receiving more lateral gust.

Gust envelopes are then produced which envelope time histories for all gust directions for a given gust length. Root torsion and root bending maximum and minimum loads are plotted in Figs. 11a and 11b, respectively. The two plots illustrate how the critical gust length (highlighted with a dot for nonlinear and cross for linear results) generally increases with flexibility. Furthermore it can be seen that the linear results typically over predict these loads, along with the critical gust length. The maximum and minimum root loads can be determined over each gust length and gust orientation and plotted for each flexibility factor and plotted in Figure 12, comparing the nonlinear, linear and linearised results, as well as the linear RTC and linearised RTC gust envelopes. It can be seen that the linear results over-estimate vertical shear, F_z,

(a) Root Torsion Moment, M_x, maximum and minimum (absolute) for all gust lengths for the stiffest and most flexible cases considered

(b) Root Bending Moment, M_y, maximum and minimum (absolute) for all gust lengths for the stiffest and most flexible cases considered

Figure 10: Maximum and minimum root loads for different gust directions on the nonlinear system (comparing the stiffest case to the most flexible case). The radial coordinate refers to the load, and the angular coordinate refers to the gust direction

torsion, M_x, and bending, M_y, but greatly underestimate axial force, F_x, fore-aft shear, F_y, and in-plane bending M_z. Results of the linearised simulations can be seen to give a much better representation of the loads. The round-the-clock loads for both the linear and linearised simulations barely exceed the linear and linearised envelopes, respectively, and therefore the lines almost coincide.

Finally, the total loads distributions (1D envelopes) are produced, which are the maximum and minimum loads for all gust lengths and gust directions, and plotted as maximum and minimum bands for each flexibility variant considered in Figure 13. It can be seen how as the aircraft is made more flexible, the loads generally reduce in magnitude, and therefore despite large deformations of the most flexible case considered, the effect of mass reduction was overall beneficial. Additionally, 2D plots have been plotted in Figure 14 as a convex hull of the time histories of root bending moment versus root torque to show how the envelopes decrease. The 2D plots for the nonlinear system are smaller in area than for linear, but qualitatively appear to have the same shape, indicating that the large deformations in this particular nonlinear system do not lead to any significant bend/twist couplings.

| Flexibility Factor | Effect of Flexibility on Nonlinear Loads | | Linear vs. Nonlinear | |
	Max Root Torque, M_x (% baseline)	Max Root Bending Moment, M_y (% baseline)	Max Root Torque, M_x (% respective nonlinear result)	Max Root Bending Moment, M_y (% respective nonlinear result)
2	11.83	9.96	7.11	1.71
1 (Baseline)	0.00	0.00	7.66	1.80
0.5	-7.30	-11.33	7.48	2.09
0.25	-11.98	-21.75	6.81	2.33
0.1	-15.38	-32.36	5.24	2.95
0.025	-17.47	-40.63	3.51	3.42

Table 2: Comparison of a selection of key loads

The results for root torque and root bending moment are summarised and quantified in Table 2. Here,
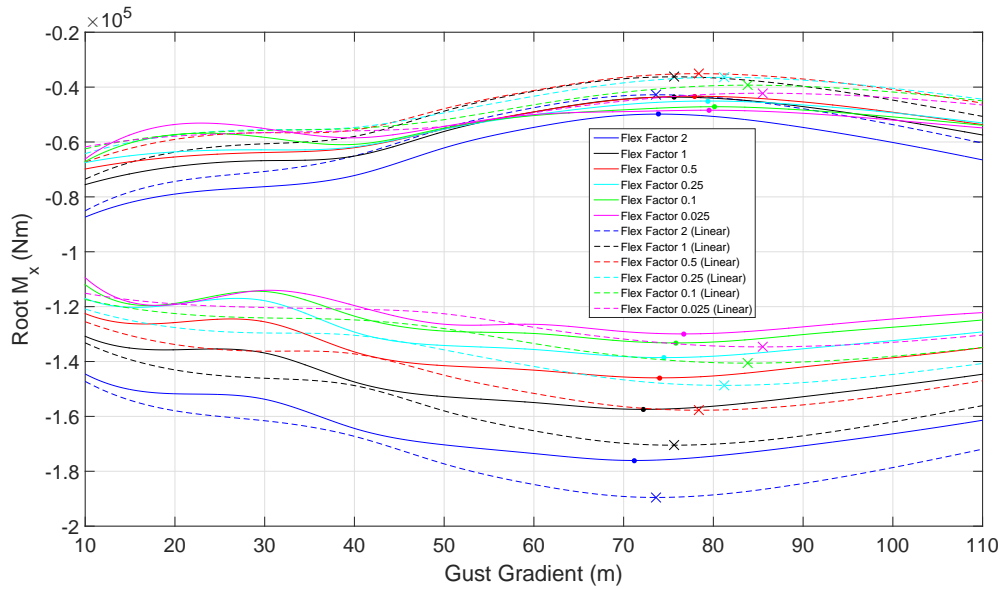
(a) Maximum and minimum root torque, M_x, per gust gradient
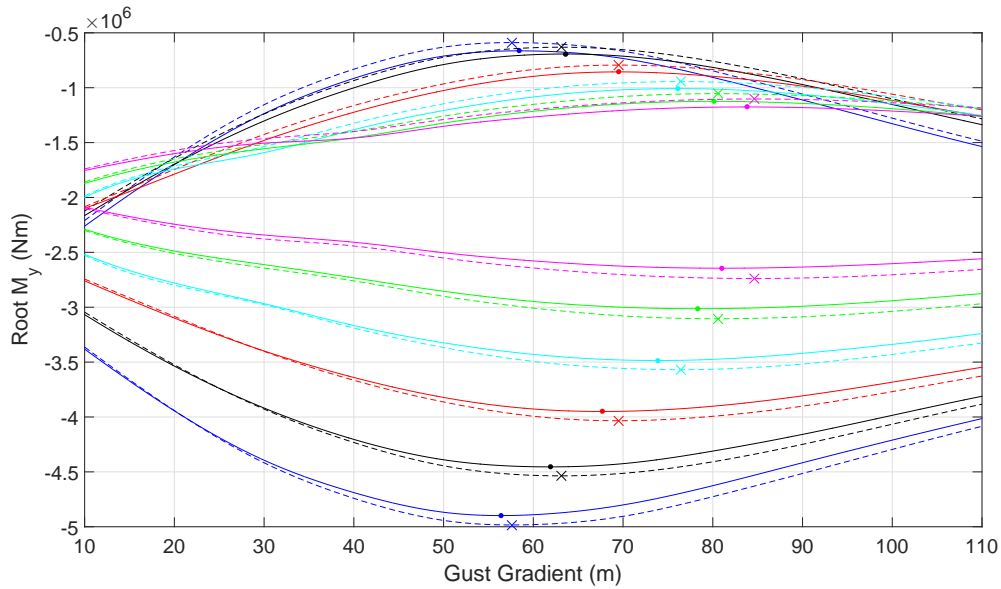
(b) Maximum and minimum root bending moment, M_y, per gust gradient

Figure 11: Maximum and minimum local root loads vs. gust gradient (dots represent the maximum nonlinear result, crosses represent the maximum linear result)

nonlinear results for different flexibility variants are compared to the baseline, and additionally the linear results are compared to those obtained from the nonlinear analyses. It can be seen that the most flexible variant of the aircraft experiences a reduction in maximum root torque of around 17.47%, and an even greater reduction of 40.63% in maximum root bending moment when compared to the maximum loads of the baseline model. Further to this, it can be seen how the maximum root bending is over-predicted using the linear methods, but only by a few percent even for the most flexible case. Root torque is also over-predicted by the linear methods, but by a larger percentage than for the root bending moment. Interestingly, the linear root torque predictions appear to be least representative of the nonlinear for the baseline case (over-predicting by 7.66%), with the percentage difference reducing as the aircraft wing becomes more flexible; in actual fact

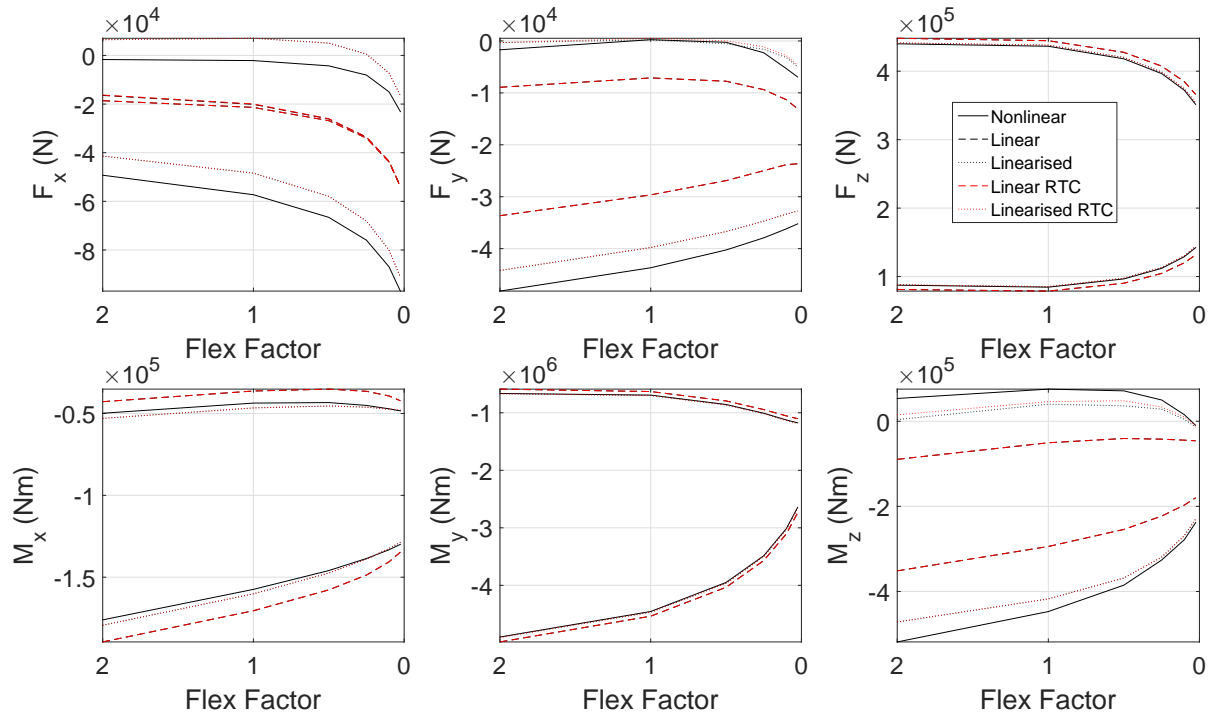American Institute of Aeronautics and Astronautics

Figure 12: Maximum and minimum local root loads vs. flexibility factor (see Figure 2 for load directions)

this is coincidental, and the linear model is not generally becoming better at predicting the nonlinear loads.

V.   Conclusions

A passenger airliner featuring HARWs has been designed and sized, and variants of this aircraft have then been generated in order to study the effects of reducing the skin thickness of the baseline design on the loads due to discrete 1MC gust disturbances.

From the static analyses it can be seen how the behaviour of the nonlinear system matches the linear approach used in MSC.NASTRAN well, with good agreement in terms of trim geometry, angle of attack and loads. As the aircraft wing stiffness is reduced, it is clear that the linear and nonlinear approaches no longer match. Additionally, it can be seen how due to nonlinearities and differences in aerodynamics and gravity modelling, the nonlinear approach predicts significant axial and fore-aft shear components, which are zero according to MSC.NASTRAN; such effects could potentially add considerably to the wing stresses.

From the dynamic analyses, it can be seen that as the aircraft is made more flexible and the structural mode frequencies reduce, the critical gust length gets longer. Also, the wing root torque and root bending moment reduce drastically with wing flexibility, with a reduction of around 17% and 41%, respectively, for the most flexible variant when compared to the original, baseline aircraft. Linear approaches over-predict root vertical shear, torque and bending moment, and the critical gust length. The root bending moment, in this case, was over-predicted by a around 3% for the most flexible case, whereas torque was over predicted by nearly 8% in some cases. Conversely, axial forces, fore-aft shear and fore-aft bending are under-predicted by the linear approach. Furthermore, the loads obtained from the linearised system were close to the nonlinear results, even in the load directions poorly predicted by the purely linear analysis. Despite large deformations, the round-the-clock gusts do not considerably exceed the envelope for most loads on the most flexible cases; most loads envelopes were formed by purely vertical gusts.

The analysis in this paper is intended to be used as part of an optimisation and design strategy using nonlinear aeroelastic modelling. As such, the method that was used in this work to produce the highly flexible variants by skin thickness reductions may result in large structural stresses, but an optimisation using this kind of procedure to determine gust loads could be created in the near future to design a HARW that uses
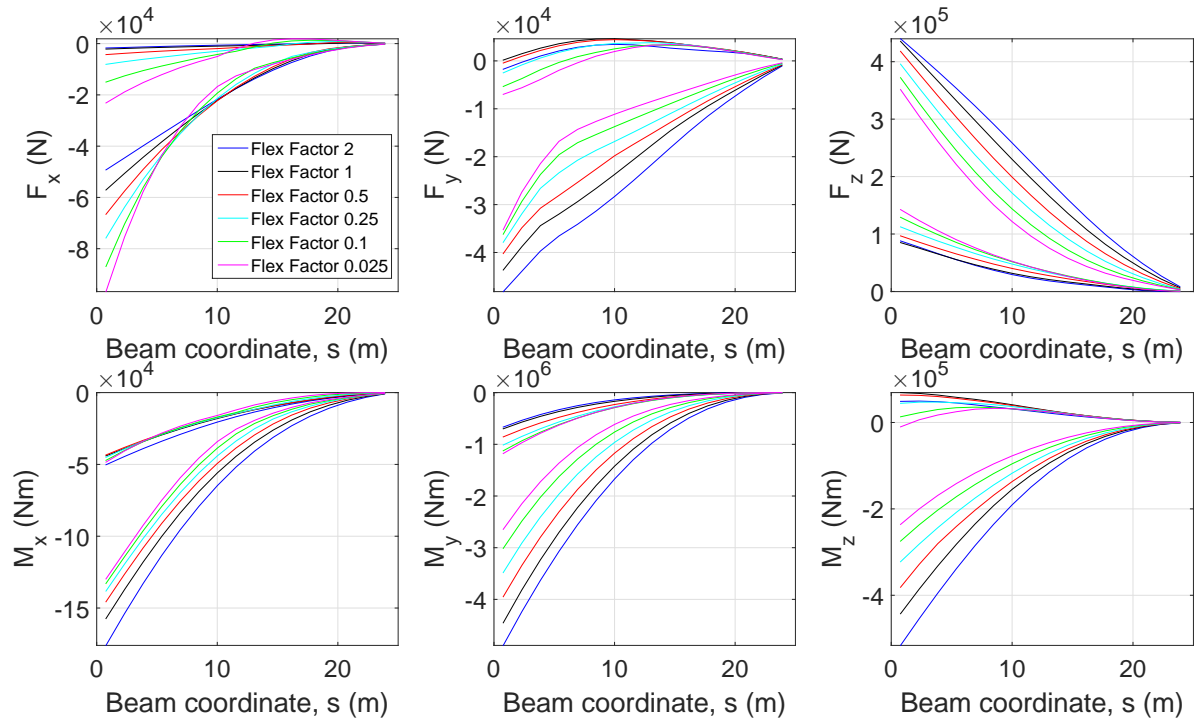
Figure 13: Maximum and minimum local gust loads vs. local beam coordinate (see Figure 2 for load directions)

large deformations as a load alleviation strategy. In this approach, the stiffness properties of portions of the wing, rather than the whole wing, could be optimised to ensure maximum stress constraints are not exceeded while still allowing for large wing displacements.

Acknowledgments

References

[1] The Airbus Concept Plane. www.airbus.com/innovation/future-by-airbus/the-concept-plane/the-airbus-concept-plane.

[2] Timothy J. Allen, Bradley W. Sexton, and Matthew J. Scott. SUGAR Truss Braced Wing Full Scale Aeroelastic Analysis and Dynamically Scaled Wind Tunnel Model Development. In *56th AIAA/ASCE/AHS/ASC Structures, Structural Dynamics, and Materials Conference*, Kissimmee, Florida, 2015.

[3] M. K. Bradley and C. K. Droney. Subsonic ultra green aircraft research. *NASA/CR-2011-216847*, 2011.

[4] D. H. Hodges. A mixed variational formulation based on exact intrinsic equations or dynamics of moving beams. *International Journal of Solids and Structures*, 26(11):1253–1273, 1990.

[5] R. Palacios, J. Murua, and R. G. Cook. Structural and aerodynamic models in the nonlinear flight dynamics of very flexible aircraft. *AIAA Journal*, 48(11):2648–2659, Nov 2010.

[6] M. Géradin and A. Cardona. *Flexible Multibody Dynamics - A Finite Element Approach*. Wiley, Chichester, England, U.K., 2001.

[7] C. E. S. Cesnik and E. L. Brown. Modeling of high aspect ratio active flexible wings for roll control. In *43rd AIAA/ASME/ASCE/AHS/ASC Structures, Structural Dynamics, and Materials Conference*, Denver, Colorado, 2002.

[8] D. H. Hodges, X. Shang, and C. E. S. Cesnik. Finite element solution of nonlinear intrinsic equations for curved composite
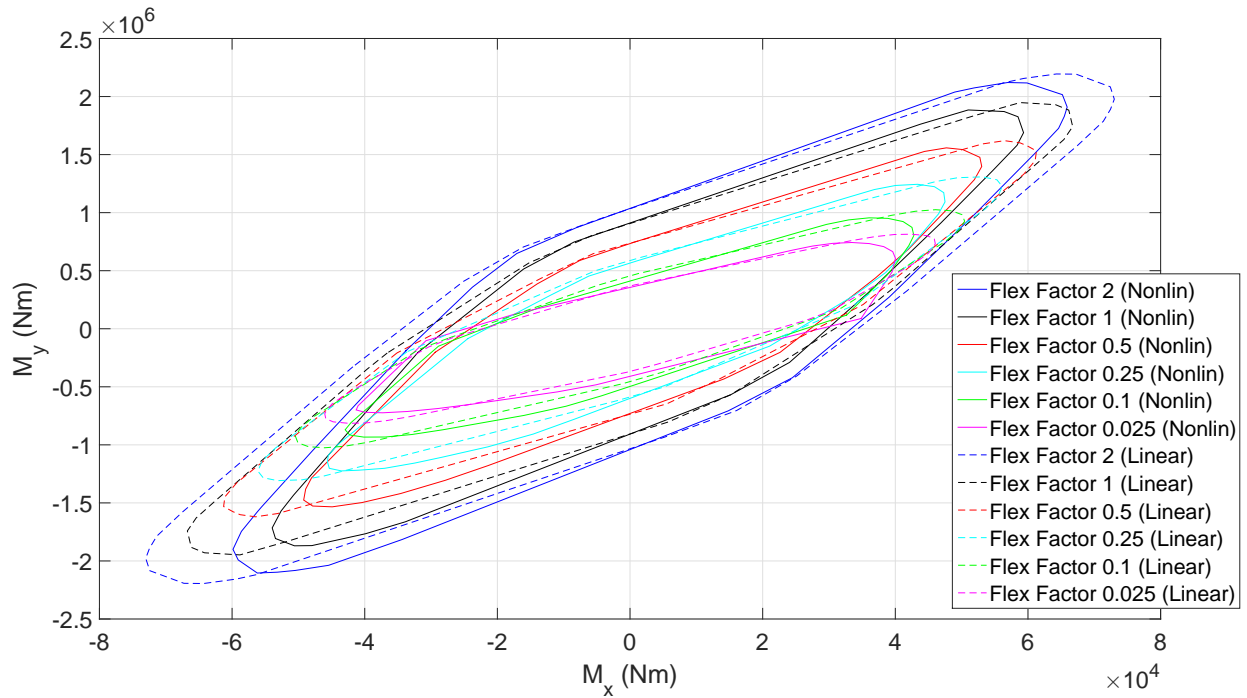
Figure 14: Root Bending Moment, M_y, vs. Torque, M_x, 2D Plot

beams. *Journal of the American Helicopter Society*, 41(9), 1996.

[9]H. Howcroft, R. G. Cook, D. E. Calderon, L. A. Lambert, M. Castellani, J. E. Cooper, M. H. Lowenberg, S. A. Nield, and E. B. Coetzee. Aeroelastic Modelling of Highly Flexible Wings. In *57th AIAA/ASCE/AHS/ASC Structures, Structural Dynamics, and Materials Conference*, San diego, California, 2016.

[10]J. G. Leishman. Unsteady lift of a flapped airfoil by indicial concepts. *Journal of Aircraft*, 31(2):288–297, 1994.

[11]W. P. Jones. Aerodynamic forces on wings in nonuniform motion. *ARCR & M 2117*.

[12]D. A. Peters, S. Karunamoorthy, and W. Cao. Finite state induced flow models. part 1: Two-dimensional thin airfoil. *Journal of Aircraft*, 32(2):313–322, 1995.

[13]J. R. Wright and J. E. Cooper. *Introduction to Aircraft Aeroelasticity and Loads*. Wiley.

[14]FAA Federal Aviation Regulations, Section 25.341. `http://www.flightsimaviation.com/data/FARS/part_25-341.html`. Accessed: 2016-10-21.

[15]EASA Certification Specifications for Large Aeroplanes, CS 25. `https://www.easa.europa.eu/system/files/dfu/CS-25_Amdt%203_19.09.07_Consolidated%20version.pdf`. Accessed: 2016-10-21.

[16]T. M. Kier. Comparison of unsteady aerodynamic modelling methodologies with respect to flight loads analysis. In *AIAA Atmospheric Flight Mechanics Conference and Exhibit*, San Francisco, California, 2005.

American Institute of Aeronautics and Astronautics